Exploring the effects of high-velocity flows in abundance determinations in H II regions. Bidimensional spectroscopy of HH 204 in the Orion Nebula[⋆]

M. Núñez-Díaz†[1,2], A. Mesa-Delgado[1,2,3], C. Esteban[1,2], L. López-Martín[1,2], J. García-Rojas[1,2] and V. Luridiana[1,2]

[1] *Instituto de Astrofísica de Canarias (IAC), E-38200 La Laguna, Tenerife, Spain*
[2] *Dept. Astrofísica, Universidad de La Laguna (ULL), E-38206 La Laguna, Tenerife, Spain*
[3] *Departamento de Astronomía y Astrofísica, Facultad de Física, Pontificia Universidad Católica de Chile,*
  Av. Vicuña Mackenna 4860, 782-0436 Macul, Santiago, Chile

ABSTRACT

We present results from integral field optical spectroscopy with the Potsdam Multi-Aperture Spectrograph of the Herbig-Haro (HH) object HH 204, with a spatial sampling of 1×1 arcsec^2. We have obtained maps of different emission lines, physical conditions and ionic abundances from collisionally excited lines. The ionization structure of the object indicates that the head of the bow shock is optically thick and has developed a trapped ionization front. The density at the head is at least five times larger than in the background ionized gas. We discover a narrow arc of high $T_e([N\ II])$ values delineating the southeast edge of the head. The temperature in this zone is about 1,000 K higher than in the rest of the field and should correspond to a shock-heated zone at the leading working surface of the gas flow. This is the first time this kind of feature is observed in a photoionized HH object. We find that the O^+ and O abundance maps show anomalous values at separate areas of the bow shock probably due to: a) overestimation of the collisional de-excitation effects of the [O II] lines in the compressed gas at the head of the bow shock, and b) the use of a too high $T_e([N\ II])$ at the area of the leading working surface of the flow.

Key words: ISM: abundances – ISM: Herbig-Haro object – ISM: individual: Orion Nebula – ISM: individual: HH 204

1 INTRODUCTION

Herbig-Haro (HH) objects were originally discovered as knots of optical emission, found in regions of low-mass star formation (Herbig 1951; Haro 1952). However, they are now observed in all spectral domains and are also associated with high-mass star-forming regions (Martí, Rodríguez & Reipurth 1993). They are often found in groups, arranged in linear or quasi-linear structures, frequently with aligned proper motion vectors (Herbig & Jones 1981; Reipurth, Raga & Heathcote 1992; Eislöffel, Mündt & Böhm 1994) and are a manifestation of the collimated supersonic ejec-

tion of material from young stars or their close circumstellar environment. HH objects show an emission line spectrum characteristic of shockwaves, with velocities typically in the range $50 - 200$ km s^{-1} (Schwartz & Dopita 1980) and, in many cases, individual knots or groups of knots have shapes that are very suggestive of bow shocks.

There are many HH objects identified in the Orion Nebula – the nearest high-mass star-forming region– which is the most observed and studied Galactic H II region. The most prominent high-velocity feature in the nebula is the Becklin-Neugebauer/Kleinmann-Low (BN/KL) complex, which contains several HH objects. In addition, there are other important high-velocity flows that do not belong to the BN/KL complex, as is the case of HH 202, 203 and 204. The origin of these flows has been associated with infrared sources embedded within the Orion-South (see O'Dell & Henney 2008a, and references therein). The hottest star in the Trapezium cluster, θ^1 Ori C (O7 V, Simón-Díaz et al. 2006), dominates
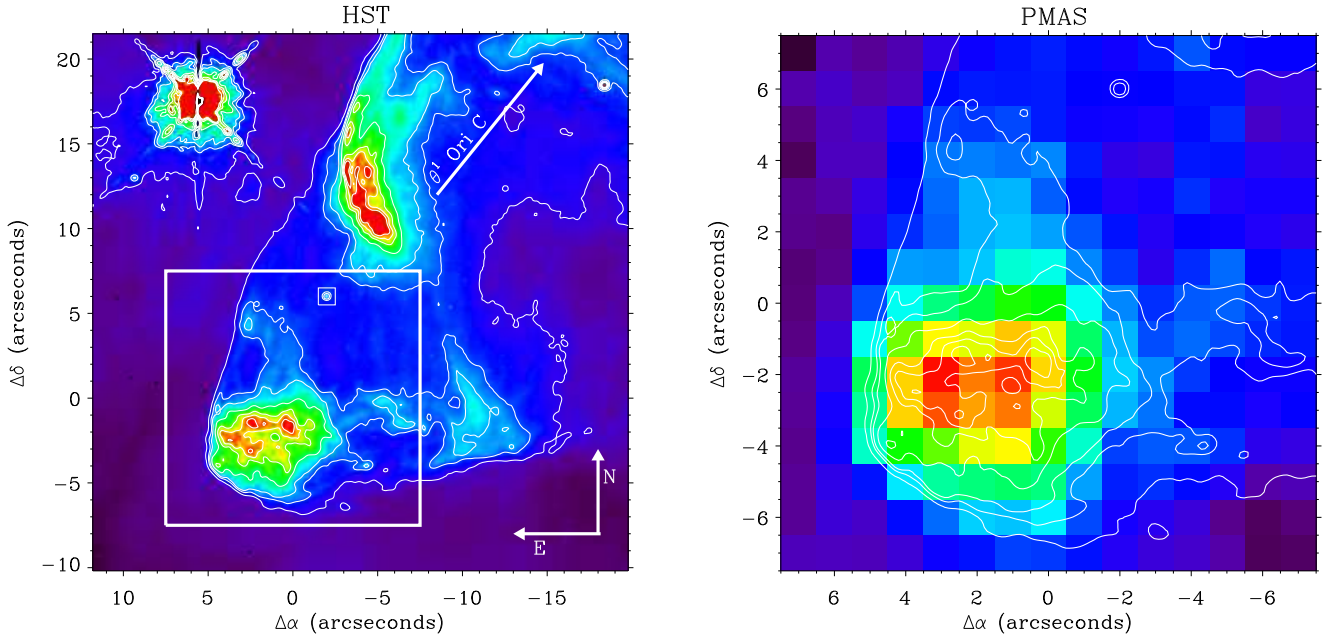
Figure 1. Left-hand side: *HST* image taken with the Wide-Field Planetary Camera 2 (WFPC2) in the narrow filter F656N (Hα+[N II]) (O'Dell & Wong 1996). The large white square corresponds to the usable PMAS FOV covering the Herbig Haro object HH 204. Right-hand side: PMAS Hα emission map with *HST* contours overplotted.

the photoionization of the surrounding gas and produces a thin blister of photoionized material. In general, the mixture of photoionized and shocked gas makes the interpretation of the spectra of HH objects within H II regions more difficult; for example, emission lines formed as a shock moves through ionized gas closely resemble those from higher velocity shock in neutral gas (Cox & Raymond 1985). Understanding line ratios in H II regions also requires distinguishing shocked from photoionized gas before we determine canonical electron temperatures and densities and ionic abundances of such regions.

HH 204 –as well as the neighbouring HH 203– is located close to θ^2 Ori A (O9 V, Simón-Díaz et al. 2006) and has an optical angular size of the order of tens of arcseconds. It was discovered by Münch & Wilson (1962) and identified as HH object by Cantó et al. (1980). It has been the subject of numerous subsequent studies of their ionization structure (O'Dell et al. 1997b), electron density (Walsh 1982), radial velocity (O'Dell, Wen & Hu 1993) and tangential motions (Cudworth & Stone 1977; Hu 1996; Doi, O'Dell & Hartigan 2002). Rosado et al. (2002), in a kinematic study based on Fabry-Pérot data, suggested that it seems to be part of a large structure or lobe. Also, these authors showed that the [O III] emission does not come from the head of the bow shock, but instead occurs primarily in a diffuse region along the southwestern portion of the object. O'Dell et al. (1997a) attribute the distribution of [O III] to differences in the way in which θ^1 Ori C illuminates this region of the nebula. The ultraviolet light from this star penetrates into the back side of the shock which moves toward the observer (O'Dell et al. 1997b)

HH 204 is a highly filamentary bright knot at the end of a rather symmetric cone that resembles a bow shock. O'Dell

et al. (1997a) indicate that the excitation in this object appears to be controlled by a mixture of local shocks and external ionization from θ^1 Ori C. It presents a pronounced asymmetry in brightness between the bow shock side near θ^2 Ori A and the side located away from this star, which is better appreciated in [N II] than in Hα. Henney (1996) has proposed that a transverse density gradient in the ambient medium where a bow shock propagates could lead to an asymmetry in brightness of the bow shock. This idea is supported by Rosado et al. (2001), who found a slight velocity gradient running perpendicular to the axis of HH 204 in the sense that the fainter (and less dense) regions show larger velocities. Originally, O'Dell et al. (1997b) interpreted that the shock of HH 204 was formed when the jet hits neutral material in the foreground Veil (O'Dell 2001), but more accurate knowledge of the position of Orion's Veil (Abel et al. 2004) and an improved determination of the trajectory of the shock allowed Doi, O'Dell & Hartigan (2004) to establish that HH 204 arises where the jet strikes denser nebular material located where the main ionization front of the Orion Nebula tilts up. This tilt is what gives rise to the Bright Bar feature that runs from northeast to southwest, passing slightly at the northwest of θ^2 Ori A.

In previous papers, our group has studied the spatial distribution and properties of the nebular gas at small spatial scales in the Orion Nebula. Using long-slit spectroscopy at spatial scales of 1.2 arcsec and crossing different morphological structures, Mesa-Delgado, Esteban & García-Rojas (2008) found spikes in the distribution of the electron temperature and density which are related to the position of proplyds and HH objects. In addition, we have published two additional studies using integral-field spectroscopy at spatial scales of 1×1 arcsec^2, focused on the analysis of

certain interesting morphological structures. Mesa-Delgado et al. (2009b) studied the prominent HH 202 and Mesa-Delgado et al. (2011) analysed areas of the Bright Bar and the northeast of the Orion South Cloud. They have mapped the distribution of the emission line fluxes and the physical and chemical properties of the nebular gas in the selected areas.

The main goal of this paper is to use integral field spectroscopy at spatial scales of 1 arcsec in order to explore the ionization structure, physical conditions and chemical abundances of one of the most remarkable HH object of the Orion Nebula: HH 204.

In Section 2 we describe the observations obtained and the reduction procedure. In Section 3 we describe the differential atmospheric refraction correction, the emission-line measurements and the reddening correction of the spectra as well as the determination of the physical conditions and chemical abundances. In Section 4 we present the spatial distribution of emission line ratios, physical conditions and chemical abundances. In Section 5 we discuss the trapped ionization front and the high-temperature arc. Finally, in Section 6 we summarize our main conclusions.

2   OBSERVATIONS AND DATA REDUCTION

The observations were made on 2008 December 20 at the 3.5m Calar Alto telescope (Almería, Spain) with the Postdam Multi-Aperture Spectrometer (PMAS, Roth et al. 2005) in service mode. The standard lens array integral field unit (IFU) was used with a sampling of $1''$ and $16'' \times 16''$ field of view (FOV). The blue range (3500 to 5100 Å) and red range (5700 to 7200 Å) were covered with the V600 grating using two grating rotator angles: −72 and −68, respectively, with an effective spectral resolution of 3.5 Å. The blue and red spectra have a total integration time of 2400 and $300s$, respectively. Additional short exposures of $30s$ were taken in order to avoid saturation of the brightest emission lines. Calibration images were obtained during the night: continuum lamp needed to extract the 256 apertures, arc lamps for the wavelength calibration and spectra of the spectrophotometric standard stars Feige 34, Feige 110 and G 191-B2B (Oke 1990) for flux calibration. The error of the absolute flux calibration of the spectra is of the order of 5%. The observing night had an average seeing of about $1.5''$.

The data were reduced using the IRAF reduction package SPECRED. After bias subtraction, spectra were traced on the continuum lamp exposure obtained before and after each science exposure, and wavelength calibrated using a Hg–Ne arc lamp. The dome flats were used to determine the response of the instrument for each fiber and wavelength. Finally, for the standard stars we have co-added the spectra of the central fibers and compared them with the tabulated one-dimensional spectra.

On the left-hand side of Fig. 1, we show a high resolution Hubble Space Telescope (*HST*) image taken with the Wide-Field Planetary Camera 2 (WFPC2) in the narrowband filter F656N (Hα + continuum) retrieved from its public archive. Two images were combined using the task *crrej* of the *hst_calib.wfpc* package of IRAF to reject cosmic rays. To locate precisely the PMAS FOV on the *HST* image, we have used the star marked with a small white box in Fig. 1
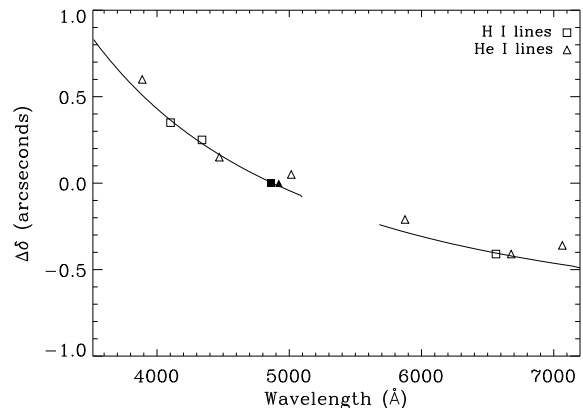
Figure 2. Comparison between the differential atmospheric refraction (DAR) values computed from Filippenko's model (solid lines) and the declination shifts obtained from our data using the CORREL_OPTIMIZE routine avaible in the IDL Astronomy User's Library. The squares represent the shifts of the H I lines with respect to Hβ (filled) and the triangles the He I lines with respect to He I 4921 Å (filled). The gap in the continuous line shows the part of the optical spectrum do not covered with the blue and red ranges of our observational setup. The symbols in the red range have been shifted −0.20 arcseconds (see text).

(left), which is visible in the spaxel $(-2, 6)$ in all the continuum maps of the PMAS field. Therefore, the accuracy in the location of the usable PMAS FOV (the large white box on the *HST* image) is better than $1''$. With the *HST* image, we computed high-resolution contours and overplotted them on all maps. Note that the resolution of the *HST* image is roughly one order of magnitude better than the PMAS one (see right-hand side of Fig. 1).

3   ANALYSIS

3.1   DAR correction

The effect of the differential atmospheric refraction (DAR) can be noticed in the data. We have used the monochromatic images of H I and He I emission lines at different wavelengths –using Hβ and He I 4921 Å as references– to correct for this effect. With the CORREL_OPTIMIZE routine avalaible in the IDL Astronomy User's Library we computed the optimal pixel offset of the monochromatic image of each selected line relative to its reference by maximizing the correlation function. In Figure 2 we represent the displacements in declination due to the DAR compared with the results of Filippenko's model (Filippenko 1982) and with respect to Hβ and He I 4921 Å. As the optical spectra analyzed are separated in two spectral ranges, there is an additional fixed instrumental shift between the lines of the red and blue ranges. This shift has been double checked using the pair of images Hα−Hβ and He I 4921 − 6678 Å, yielding displacements of $(0.10, -0.20)$ and $(0.10, -0.25)$ pixels, respectively. We chose the first pair of values because it is computed with much brighter lines. Therefore, the displacements of lines in the red range of the spectrum have been shifted $(0.10, -0.20)$ arcsecs. Figure 2 only presents the behaviour of DAR in the declination axis because it has larger values than in right
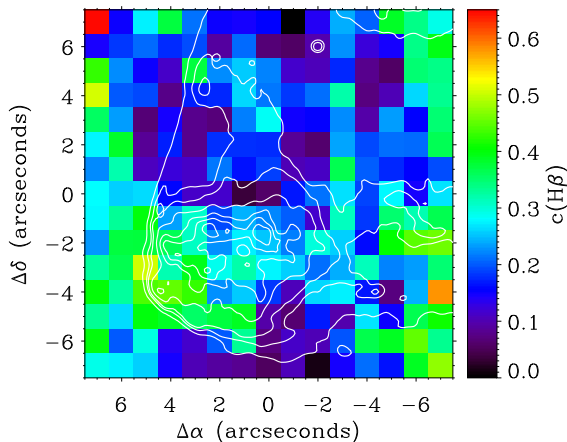
Figure 3. Spatial distribution map of the extinction coefficient, c(Hβ). The contours plotted are those from the *HST* F656N images. The size of the field corresponds to the maximal coincident FOV after correcting the spectra for differential atmospheric refraction (see text).

ascension due to the paralactic angle is better aligned with the declination axis. Attending to the good agreement of the model with the data values, we corrected from DAR the whole set of data cube applying the BILINEAR routine of IDL with a global and independent offset to each axis, in order to maximize the coincident FOV (15×15 arcsec^2).

3.2 Line intensity measurements

The emission lines considered in our analysis are the following: hydrogen Balmer lines, from Hα to H12, which are used to verify the DAR correction and to compute the reddening coefficient; collisionally excited lines (CELs) of various species, which are used to compute physical conditions and chemical abundances.

Line fluxes were measured applying a single or a multiple Gaussian profile fit procedure between two given limits and over the local continuum. All these measurements were made with the SPLOT routine of IRAF and using our own scripts to automatize the process. The associated errors were determined following Mesa-Delgado, Esteban & García-Rojas (2008). In order to avoid spurious weak line measurements, we imposed three criteria to discriminate between real features and noise: 1) Line intensity peak over 2.5 times the sigma of the continuum; 2) FWHM(H I)/1.5 < FWHM(λ) < 1.5×FWHM(H I); and 3) F(λ) > 0.0001 × F(Hβ).

All line fluxes of a given spectrum have been normalized to Hβ and Hα for the blue and red range, respectively. To produce a final homogeneous set of line ratios, all of them were re-scaled to Hβ. The re-scaling factor used in the red spectra was the theoretical Hα/Hβ ratio for the physical conditions of $T_e = 10000$ K and $n_e = 1000$ cm^{-3}.

3.3 Reddening coefficient

The reddening coefficient, c(Hβ), has been obtained by fitting the observed Hγ/Hβ and Hδ/Hβ ratios to the theoretical ones predicted by Storey & Hummer (1995) for $n_e = 1000$ cm^{-3} and $T_e = 10000$ K. We have used the reddening function, $f(\lambda)$, normalized to Hβ determined by Blagrave et al. (2007) for the Orion Nebula. The use of this extinction law instead of the classical one of Costero & Peimbert (1970) produces c(Hβ) values about 0.1 dex higher and dereddened fluxes with respect to Hβ about 3% lower for lines in the range 5000 to 7500 Å and 4% higher for wavelengths below 5000 Å. The final adopted c(Hβ) value for each spaxel is an average of the individual values derived from each Balmer line ratio weighted by their corresponding uncertainties. The typical error is about 0.1 dex for each spaxel. The resulting extinction map is shown in Figure 3, where the extinction coefficient varies approximately from 0.1 to 0.6 dex. The mean value in the FOV is 0.23 dex. We have compared our c(Hβ) value with the extinction map obtained by O'Dell & Yusef-Zadeh (2000) from the Hα/Hβ line ratio using calibrated *HST* images, where HH 204 is located between the contour lines of 0.2 and 0.4 dex on that map. Therefore, we find that our mean value of the reddening coefficient is consistent with the previous determinations taking into account the errors and the different extinction laws used. However, we also find some regions with higher values of extinction than those reported by O'Dell & Yusef-Zadeh (2000). It must be said that, due to its closeness to θ^2 Ori A, the Hδ and Hγ lines of the spectra are somewhat affected by underlying absorption due to the stellar continuum reflected by dust. This may affect the measurement of the intensity of Balmer lines, especially the bluest ones, producing a slightly higher c(Hβ), and this may be the reason of such discrepancy. However, the results of our paper are not particularly sensitive to this issue.

3.4 Physical conditions

Nebular electron densities, n_e, and temperatures, T_e, have been derived from the usual CEL diagnostic ratios – [S II] 6717/6731 for n_e, and [N II] (6548+6583)/5755, [S II] (6716+6731)/(4068+4076) and [O III] (4959+5007)/4363 for T_e– and using the TEMDEN task of the NEBULAR package of IRAF with updated atomic data (see García-Rojas, Peña & Peimbert 2009). Following the same procedure as Mesa-Delgado, Esteban & García-Rojas (2008), we have assumed an initial $T_e = 10000$ K to derive a first approximation of n_e([S II]), then we calculate T_e([N II]), and iterate until convergence. We have not corrected the observed intensity of [N II] 5755 Å for contribution by recombination when determining T_e([N II]) because this is expected to be rather small in the Orion Nebula (e.g. Esteban et al. 2004). We did not use T_e([S II]) for the iteration procedure because the auroral lines of [S II] are rather weak outside HH 204 and the diagnostic line ratio involves lines located in the blue and red spectral ranges. Nevertheless, using both [S II] diagnostic ratios together the density values are in good agreement within the errors with those determined with T_e([N II]). On the other hand, because of the relatively low spectral resolution of the observations, [O III] 4363 Å is somewhat blended with the Hg I+[Fe II] 4358 Å lines. The latter one becomes

very strong inside the HH object. Only in this case, we performed manually the Gaussian fit of those three lines in order to obtain a good determination of $T_e([O\,\textsc{iii}])$. The automatic procedure gave some inconsistent values at the northeast corner of the FOV because of the faintness of the [O\,\textsc{iii}] 4363 Å line in that area. The typical uncertainties in the density maps range from 200 to 2000 cm^{-3}. The errors for electron temperatures range from 150 to 350 K for $T_e([N\,\textsc{ii}])$, from 100 to 400 K for $T_e([O\,\textsc{iii}])$ and from 100 to 500 K for $T_e([S\,\textsc{ii}])$.

3.5 Chemical abundances

The IRAF package NEBULAR has been used to derive ionic abundances of S^+, N^+, O^+ and O^{2+} from the intensity of CELs. We have assumed no temperature fluctuations in the ionized gas ($t^2 = 0$) and a two-zone scheme: $T_e([N\,\textsc{ii}])$ is used to derive the S^+, N^+ and O^+ –the low ionization potential ions– and $T_e([O\,\textsc{iii}])$ for the O^{2+} abundances. The uncertainties in ionic abundances have been calculated as a quadratic sum of the independent contributions of errors in n_e and T_e. For oxygen abundances, the uncertainties are $0.04-0.08$ dex for O^+, $0.02-0.05$ dex for O^{2+} and $0.02-0.06$ dex for O.

4 RESULTS: SPATIAL DISTRIBUTION MAPS

In this section we analyse the spatial distributions of several emission line ratios, electron densities and temperatures as well as several representative ionic and total abundances.

4.1 Ionization structure

In Fig. 4, we show the line intensity ratio maps of [O\,\textsc{i}] 6300 Å, [S\,\textsc{ii}] 6731 Å, [O\,\textsc{ii}] 3727 Å, [N\,\textsc{ii}] 6583 Å, [Fe\,\textsc{iii}] 4881 Å, [S\,\textsc{iii}] 6312 Å, He\,\textsc{i} 6678 Å, [O\,\textsc{iii}] 5007 Å and [Ne\,\textsc{iii}] 3868 Å relative to Hβ. The minimum and maximum values of the color bars of the different ratios have been rescaled to show the same dynamical range in all the maps. The dynamical range of reference adopted is that of the [O\,\textsc{i}]/Hβ ratio, which shows the largest variation. The selected lines cover all possible ionization conditions of the gas. The maps are sorted from lower (top-left) to higher (bottom-right) ionization potential. These line ratios are directly related to the local ionization degree of the gas and do not depend on density in a direct manner.

[O\,\textsc{i}] 6300 Å is a strong line in shocks, but is rather weak in photoionized regions (e.g. Masciadri & Raga 2001). However, this line can also be a tracer of the presence of trapped ionization fronts (as in the case of HH 202, in the Orion Nebula: Mesa-Delgado et al. 2009a,b). In Fig. 4a, we can see that [O\,\textsc{i}]/Hβ is much higher in the southeast quadrant of the bow shock and very low along the bow shock wings. This indicates that the wings of the flow are completely photoionized. In order to disentangle the excitation mechanism of the gas at the bow shock, we have represented its [O\,\textsc{i}]/Hα and [O\,\textsc{i}]/[O\,\textsc{iii}] ratios on a diagnostic diagram adapted from Riera, Phillips & Mampaso (1990) that separates shock excitation from photoionization, finding that it is esentially photoionized, and that no substantial contribution of shock

excitation is needed to reproduce its spectrum. In their models of optically thick HH objects inside photoionized regions, Masciadri & Raga (2001) find that trapped ionization fronts restricted at the head of the bow shock show an [O\,\textsc{i}]/Hβ ratio concentrated to the side directed away from the ionizing photon source, exactly what we see in Fig. 4a. The [S\,\textsc{ii}] line emission is also a tracer of ionization fronts. In Fig. 4b, we can see that [S\,\textsc{ii}]/Hβ follows rather closely the distribution of [O\,\textsc{i}]/Hβ.

As we can see in Fig. 4c and 4h, the distribution of [O\,\textsc{ii}]/Hβ shows an almost inverse behaviour with respect to [O\,\textsc{iii}]/Hβ presenting its lowest values at the western part of the FOV, exactly where the [O\,\textsc{iii}]/Hβ ratio is higher. However, [O\,\textsc{iii}]/Hβ reaches its minimum at the head of the bow shock while [O\,\textsc{ii}]/Hβ does not present peak values at those spaxels. This indicates that the spatial distribution of [O\,\textsc{ii}] 3727 Å and Hβ is rather similar at the bow shock.

The [N\,\textsc{ii}]/Hβ ratio (Fig. 4d) reaches its maximum at the bow shock, and delineates the wings of the flow structure. It can also be seen that the area closer to the star θ^2 Ori A is brighter than the rest. This result is in agreement with Rosado et al. (2001), who reported that the asymmetry in the brightness distribution of HH 204 is better appreciated in [N\,\textsc{ii}] than in Hα.

HH objects are also characterized by their strong emission in [Fe\,\textsc{iii}] lines. In Fig. 4e, we can see the spatial distribution of the [Fe\,\textsc{iii}]/Hβ ratio where the maximum values seem to be concentrated just behind the areas of the maxima of the [O\,\textsc{i}]/Hβ and [S\,\textsc{ii}]/Hβ ratios. The high [Fe\,\textsc{iii}] emission may be related to destruction of dust grains due to the passage of shock waves as in the case of HH 202 (Mesa-Delgado et al. 2009a,b).

The spatial distributions of [S\,\textsc{iii}]/Hβ and He\,\textsc{i}/Hβ are rather similar and smooth (Fig. 4f, g). Higher values tend to be concentrated toward the west of the FOV. This concentration is more evident in the higher ionized species [O\,\textsc{iii}]/Hβ and [Ne\,\textsc{iii}]/Hβ (Fig. 4h, i) due to the contrast between the minimum and maximum line ratios is more pronounced. It is important to comment that the high excitation lines of [O\,\textsc{iii}] and [Ne\,\textsc{iii}] do not form at the head of the bow shock like they usually do in other HH objects produced by high-velocity flows, but instead occur primarily in the ambient diffuse background across the western portion of the FOV. This distribution is attributed to differences in the way in which the star θ^1 Ori C illuminates this zone of the nebula (O'Dell et al. 1997b) and the relatively large distance between the star and HH 204, which makes the impinging ionizing flux too low to maintain the presence of a substantial fraction of O^{2+} ions at the bow shock.

4.2 Physical conditions

In Fig. 5 we present the physical conditions determined for the observed field, where the head of the bow shock is associated with local peaks of electron density.

Fig. 5a shows the $T_e([N\,\textsc{ii}])$ map. A remarkable feature is the narrow high-temperature zone just at the southeast border of the head of the bow shock. This structure seems to be real, since the temperature determination has only an error of about 2%, much lower than the temperature increase. Furhtermore, it is a rather narrow feature that can only be distinguished when the DAR correction is applied. On the
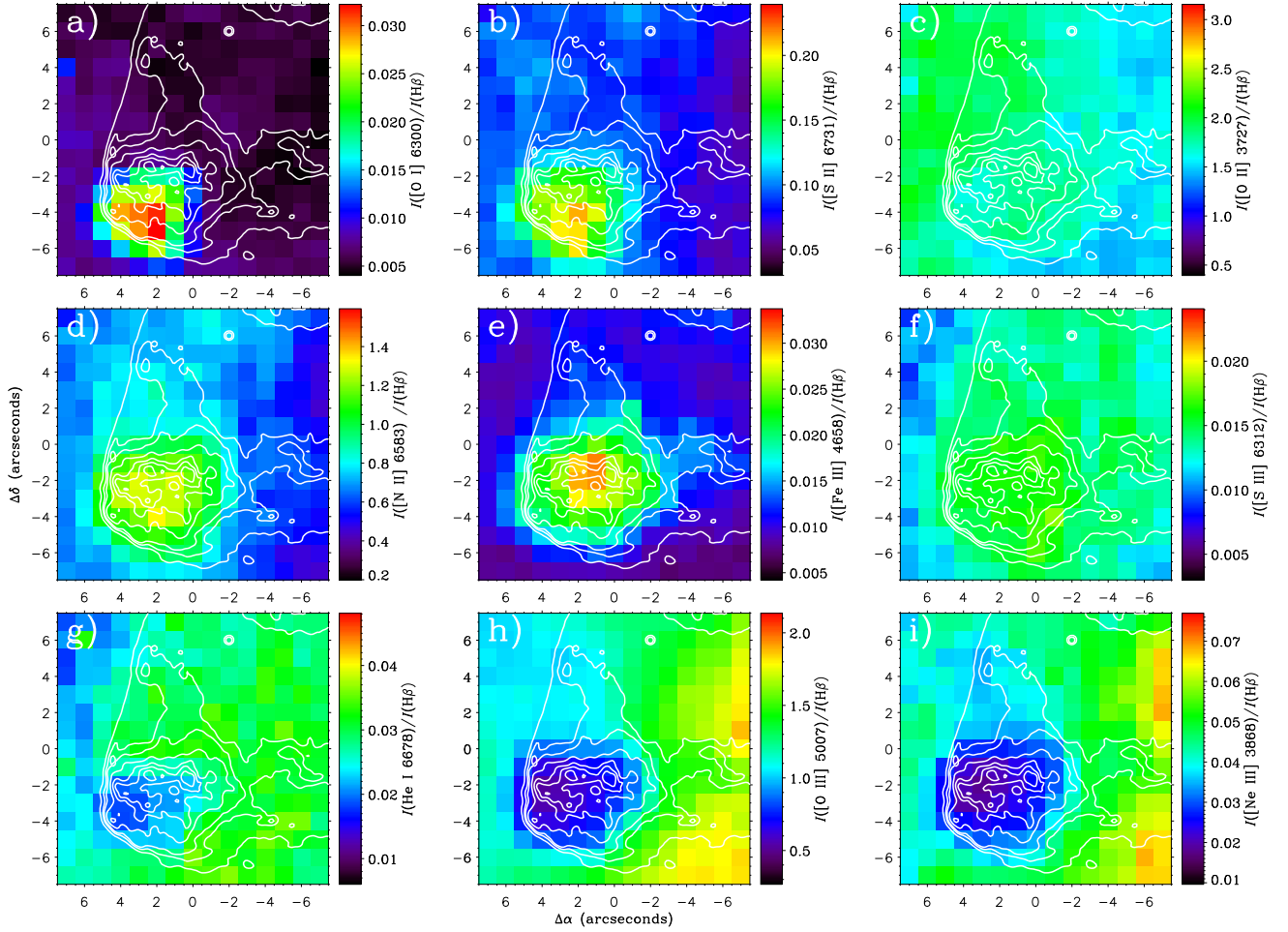
Figure 4. Maps of line intensity ratios relative to Hβ of selected emission lines: a) [O I] 6300 Å, b)[S II] 6731 Å, c) [O II] 3727 Å, d) [N II] 6583 Å, e) [Fe III] 4658 Å, f) [S III] 6312 Å, g) He I 6678 Å, h) [O III] 5007 Å and i) [Ne III] 3868 Å. The contours plotted are those from the *HST* F656N images. The color bars have been re-scaled to have the same dynamical range between the maximum and minimum values in all maps.

other hand, this high-temperature zone cannot be produce by the slight extinction excess we find in a nearby –but not coincident– area of the head. We would need c(Hβ) differences by about unity to account for a temperature increase of 1000 K. We also do the exercise of correcting the whole set of data with two constant values of c(Hβ), 0.2 and 0.4 dec, and the high-temperature arc is still clearly present in both cases. Then the derived temperature enhancement is not an artifact of the high local extinction. The nature of this structure will be discussed later. Fig. 5b shows the n_e([S II]) map derived in combination with T_e([N II]) until convergence. Assuming this initial n_e([S II]) map we also derived the T_e([S II]) map (see Fig. 5e), which shows an arc that delineates a zone of strong increase of temperature at the northeast of the head. We found that this structure also appears if we calculate the map of the S$^+$ abundances derived from the auroral [S II] lines when using T_e([N II]) (Fig. 5a) and n_e([S II]) (Fig. 5b). Obviously, that result has no physical meaning. The simpler explanation for this fact is that we are not using appropriate values of the electron density for deriving S$^+$ abundances and this affects especially the calculations based on nebular [S II] lines, which have lower

critical densities than the auroral ones. In order to correct for this discrepancy in the S$^+$ abundance, we determined the n_e([S II]) map that –assuming the T_e([N II]) distribution of Fig. 5a– makes the differences between the abundance obtained from the nebular and auroral lines lower than the estimated maximum error of this abundance, ±0.08 dex. The final electron density map is shown in Fig. 5c, where only half of the spaxels show values different from the previous map. It must be said that using an iterative procedure in which both T_e([N II]) and n_e([S II]) are changed we do not find a substantially different final T_e([N II]) map because the [N II] lines involved in the temperature indicator have critical densities much higher than the n_e([S II]) values we are obtaining for HH 204. In Fig. 5c we can see that this new density map fits much better the Hα contours not only inside the head of the bow shock, but also at the location of other structures visible in the *HST* images such as the wing at the west of the head. We recomputed T_e([S II]) assuming the n_e([S II]) map of Fig. 5c and obtained the distribution showed in Fig. 5f, finding a much smoother map where the arc-shaped area of very high temperatures has disappeared.
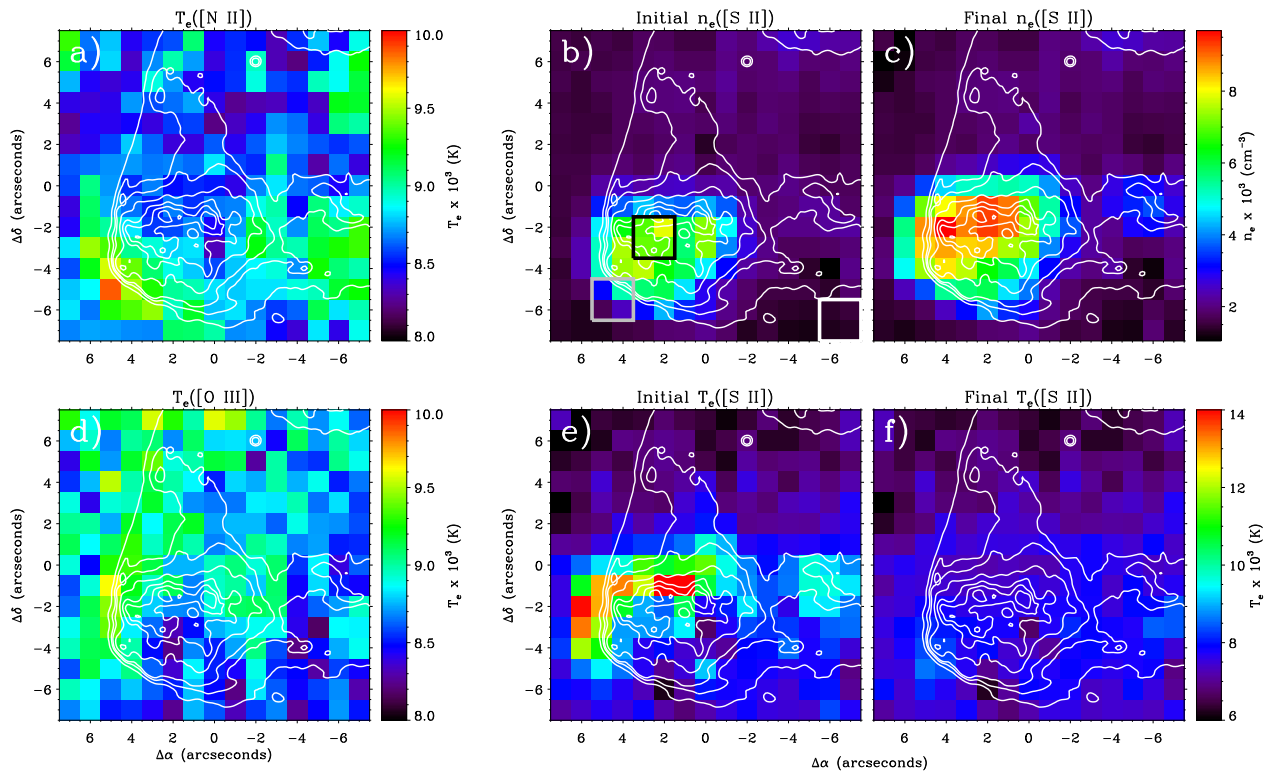
Figure 5. Physical conditions of HH 204 a) T_e([N II]), b) and c) two different estimates of n_e([S II]), d) T_e([O III]), e) and f) two different estimates of T_e([S II]). See text for details. The contours plotted are those from the *HST* F656N images. In the density map b) we mark three different zones: background gas (white box), head of the bow shock (black box) and high-temperatutre arc (grey box), whose spaxels have been co-added in order to analyse their spectra and derive the physical conditions at those zones.

The final n_e([S II]) map of Fig. 5c is the one we have used to derive the chemical abundances.

In Fig. 5c we can see that the highest densities in the FOV are between 4000 and 9000 cm^{-3}. Similar values were obtained by Mesa-Delgado, Esteban & García-Rojas (2008) from a slit crossing HH 204 and roughly parallel to the direction toward θ^1 Ori C (see Fig. 7). The density map shows the highest values at the roundish clumpy structure of the head of the bow shock while the extended wings show densities only slightly higher than those of the surrounding background gas. The lowest density values ($n_e < 2000$ cm^{-3}), related to the background gas, are located at the southwest edge of both FOV. We obtained an additional density determination making use of the [Fe III] lines. We detected at least 5 [Fe III] lines of the 3F multiplet ([Fe III] 4607,4658, 4702, 4734 and 4755 Å) and one line of the 2F multiplet ([Fe III] 4881 Å) at those spaxels at the head of the bow shock showing the maximum values of n_e([S II]). The range of validity of this density indicator, n_e([Fe III]), has an upper limit well above 10^6 cm^{-3}. To carry out these calculation we have used a 34-level atom using the collision strengths from Zhang (1996) and the transition probabilities of Quinet (1996) and Johansson et al. (2000). The calculations of n_e([Fe III]) give densities varying from 8000 to 15000 cm^{-3}, but the uncertainties are rather large due to the faintness of the [Fe III] lines. Therefore, the n_e([S II]) values we obtain in Fig. 5c should be considered a fair approximation to the true electron density of the ionized gas at HH 204. It is interesting

to comment that Solf, Böhm & Raga (1988) found a rather similar lack of correlation between auroral and nebular [S II] lines in a one-dimensional spectrum across the head of the prototypical HH 1. They also found rather high n_e([S II]) values –of the order of 3000 cm^{-3}– that peak at the head, precisely where the intensity ratio between auroral and nebular [S II] lines is higher. This behavior is also similar to that observed in our case and can also be explained by the effect of collisional deexcitation of the nebular lines.

The spatial distribution of T_e([O III]) (Fig. 5d) is rather smooth, with higher values located at the northeast edge of the FOV. This area shows the faintest [O III] 4363 Å emission and therefore have the largest errors. In fact, the anomalously high T_e of some spaxels might indicate that the [O III] 4363 Å line has not been properly deblended from Hg I+[Fe III] 4358 Å lines. There is an apparent trend of slightly higher T_e([O III]) around the northern half of the head of the bow shock.

In Fig. 5b we mark three selected areas covering different zones, whose spectra have been extracted in order to analyse their physical conditions. These areas are: background gas (white box), head of the bow shock (black box) and high-temperature arc (grey box). This last zone corresponds to the area showing the peak of T_e([N II]) located at the southeast of the head (see Fig. 5a). In Table 1, we summarize the density and temperature values we obtain for each zone. The n_e([S II]) of the three zones are very different, 1400 cm^{-3} for the background, 9000 cm^{-3} for the head and

Table 1. Physical conditions of the three selected zones (see Fig. 5b).

Zone	$c(H\beta)$ (dec)	$n_e([\text{S II}])$ (cm^{-3})	$n_e([\text{Fe III}])$ (cm^{-3})	$T_e([\text{N II}])$ (K)	$T_e([\text{S II}])$ (K)	$T_e([\text{O III}])$ (K)
background	0.4 ± 0.1	1400 ± 300	2800 ± 1900	8800 ± 300	7700 ± 300	8500 ± 200
head	0.3 ± 0.1	9000 ± 1800	15300 ± 5600	8700 ± 150	7800 ± 250	8700 ± 350
high-temperature arc	0.3 ± 0.1	3800 ± 550	5000 ± 500	9600 ± 200	8500 ± 300	8800 ± 250

3800 cm^{-3} for the high-temperature arc. It is remarkable that the electron densities determined with [Fe III] lines are rather consistent with the quoted values of $n_e([\text{S II}])$ within the uncertainties and show the same qualitative behaviour. On the other hand, the electron temperature of low ionization species shows similar values in the background and the head of the bow shock and higher ones at the high-temperature arc. In the case of $T_e([\text{N II}])$ the increase is of about 1,000 K and in the case of $T_e([\text{S II}])$ it is somewhat lower, about 700 K. Finally, $T_e([\text{O III}])$ is practically the same in the three areas within the errors. These results indicate that there might be a process of extra heating in the high-temperature arc area (see Section 5.2). This process only affects to low-ionization ionic species, because – attending to the results of Section 4.1 and Section 4.3– high-ionization species –such as O^{2+}– are absent at the head of HH 204.

4.3 Chemical abundances

In the first row of Fig. 6 we present the spatial distributions of the O^+/H^+, O^{2+}/O^+ and O/H ratios derived from CELs. The O^+ abundance is strongly concentrated at the north of the head (see Fig. 6a). As we can see in Fig. 6b, the O^{2+}/O^+ ratio shows an almost inverse behaviour with respect to O^+ abundance, indicating the strong ionization stratification across the FOVs. Unexpectedly, we do not find a constant value in the spatial distribution of the total O abundance, as we can see in Fig. 6c.

The mean value of the O abundance amounts to $12+\log(O/H) = 8.40 \pm 0.04$ dex, which is slightly lower than the typical values of about 8.50 dex obtained by previous works in other parts of the Orion Nebula (Esteban et al. 1998, 2004; Blagrave, Martin & Baldwin 2006; Mesa-Delgado et al. 2009a; Simón-Díaz & Stasińska 2011). The maximum values –with abundances between 0.1 and 0.2 dex higher– are concentrated at the north half of the head where the errors are minimal and the minimum values –about 0.15 dex lower– are just at the high-temperature arc. It is remarkable that the O^+ (Fig. 6a) and O (Fig. 6c) abundance maps are almost identical, indicating that the variations of the total O abundance are produced by the structure of the O^+ abundance. A similar result has also been obtained in a previous paper of our group devoted to the analysis of PMAS data of ionization fronts in the Orion Nebula (Mesa-Delgado et al. 2011). However, in that paper and in contrast to our results for HH 204, we find that the O^+ and O maps were also similar to that of $n_e([\text{S II}])$. As we can see in Fig. 6c, the O^+ and O maps reach a minimum just at the southeast edge of the head of the bow shock –just at the position of the $T_e([\text{N II}])$ peak of Fig. 5a– and this feature does not have

any counterpart in neither the initial nor the final $n_e([\text{S II}])$ maps (Figs. 5b and c, respectively).

Considering all the aforementioned results, we propose that two different physical effects are affecting the determination of the O^+ abundance –and consequently, the total O abundance– across the field of HH 204. First, following the arguments outlined in Mesa-Delgado et al. (2011), the most likely explanation for the higher O^+/H^+ values obtained at the head is that the values we obtain for $n_e([\text{S II}])$ are higher than the true ones of the O^+ zone. Therefore, we are overestimating the collisional de-excitation of the [O II] 3727 Å lines. Taking into account the O^+/H^+ excess at the head of HH 204 and the results of Mesa-Delgado et al. (2011) we estimate that the true densities at the O^+ zone should be about 1000 cm^{-3} lower than those indicated by $n_e([\text{S II}])$. If we correct the density by that factor –which is of the order of the quoted errors– we obtain an O abundance similar to that of the background gas around HH 204. Second, the effect producing the slightly lower O^+ abundances at the high-temperature arc seems to be connected with the localized increase of $T_e([\text{N II}])$ seen in Fig. 5a. Assuming that the unexpected abundance pattern is the consequence of using an electron temperature which is higher than that expected considering thermal equilibrium of a static photoionized nebula, we have estimated by which amount we have to correct the $T_e([\text{N II}])$ values of each spaxel of the high-temperature arc to reproduce the mean nominal value of the total O abundance, 8.40 dex. The result is that, by decreasing $T_e([\text{N II}])$ by 1,000 K, we obtain the expected O abundance and the arc of high $T_e([\text{N II}])$ disappears. This result support the idea that there might be an extra heating due to shocks.

Finally, we present the N^+/H^+, N^+/O^+ and N^+/S^+ ratios in the bottom row of Fig. 6. The N^+ abundance shows a rather similar spatial distribution to that of O^+ as it is expected from their similar ionization potentials. However, the ratio between both ionic abundances shows slight spatial variations concentrated at the south edge of the head. These variations can be due to the different temperature and density dependence of the lines used to derive both ionic abundances. Finally, the N^+/S^+ ratio delineates the presence of a trapped ionization front at the head of the bow shock and the strong ionization gradient across the FOV.

5 DISCUSSION

5.1 The trapped ionization front

Most HH objects are located in molecular and neutral environments and their gas is shock-excited. However, HH 204 –like other objects such as HH 444 (see Reipurth et al. 1998), HH 505 (see Bally & Reipurth 2001), HH 529 (see Blagrave,
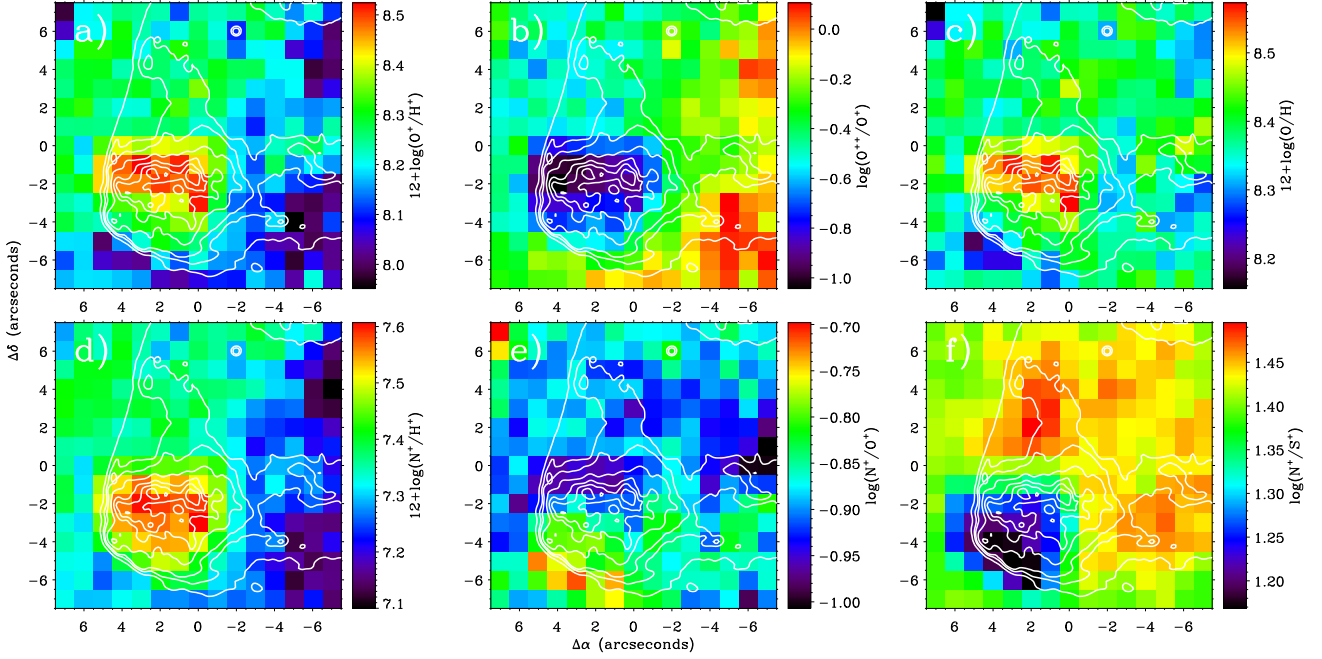
Figure 6. Ionic abundance and abundance ratio maps determined from the intensity of collisonally excited lines. From top-left to bottom-right: $12 + \log(O^+/H^+)$, $\log(O^{2+}/O^+)$, $12 + \log(O/H)$, $12 + \log(N^+/H^+)$, $\log(N^+/O^+)$ and $\log(N^+/S^+)$. The contours plotted are those from the *HST* F656N images.
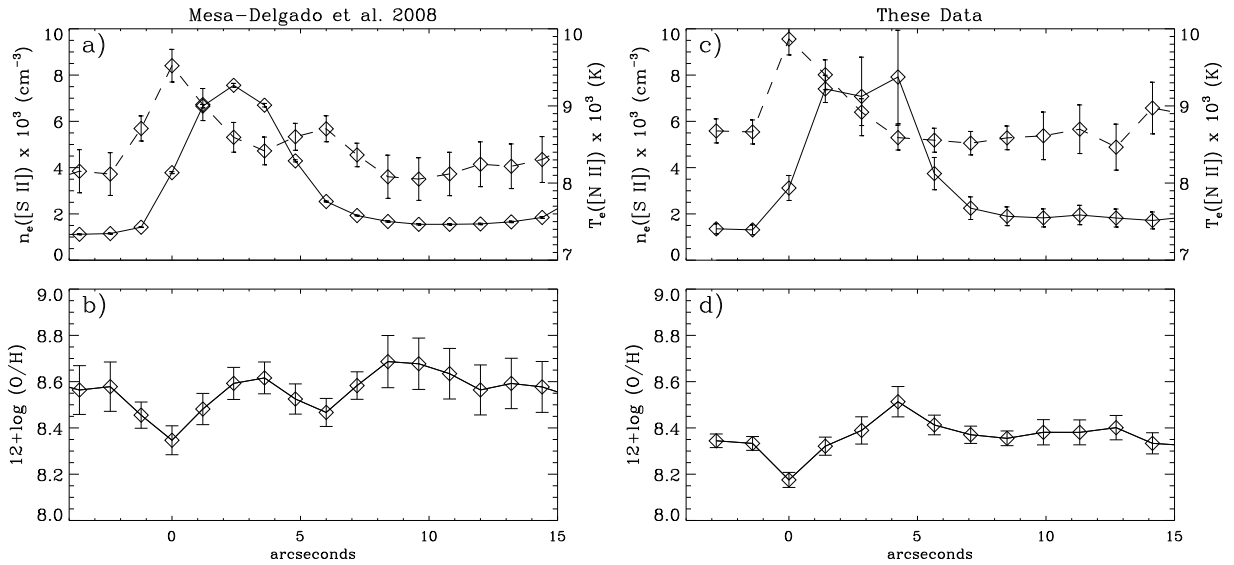

Figure 7. Spatial profiles of several parameters along slit position 3 of Mesa-Delgado, Esteban & García-Rojas (2008) crossing HH 204 on the left panels and a pseudo-slit along the main diagonal of our PMAS maps on the right. Top panels: profiles of $n_e([\text{S II}])$ (*solid line*) and $T_e([\text{N II}])$ (*dashed line*). Bottom panels: profile of the total oxygen abundance. The origin of abscissae corresponds to the peak value of $T_e([\text{N II}])$.

Martin & Baldwin 2006) or HH 202 (see Mesa-Delgado et al. 2009a)– is an example of collimated HH jet immersed in a photoionized region, where the excitation of the gas is dominated by the stellar ionizing radiation. There are rather few theoretical models that describe the structure and evolution of photoionized HH jets (e.g. Raga et al. 2000; Masciadri & Raga 2001; Raga & Reipurth 2004; Raga, Riera &

González-Gómez 2010). Our unprecedentedly detailed integral field spectroscopical observations permit to study not only the ionization structure but also the physical conditions of the gas along the head of the bow shock, something rather unusual in the literature. Therefore, our data are of paramount interest to compare with the predictions of jet models. The most suitable models for the particular condi-

tions of HH 204 are those by Masciadri & Raga (2001), who consider a source of radiation with a flux of ionizing photon comparable to that expected for θ^1 Ori C and located at different distances from the jet. Especially interesting is their model 2, in which the linear distance between the ionizing source and the jet is of the order of that of HH 204 with respect to θ^1 Ori C. An apparent drawback of our comparison with the models of Masciadri & Raga (2001) is that they consider that the direction toward the ionizing star is perpendicular to the outflow axis, whilst in our case the jet is oriented very close to the direction of θ^1 Ori C. In any case, this difference does not affect the results qualitatively.

Masciadri & Raga (2001) find that their model 2 produces a trapped ionization front at the head of the bow shock while the wings are completely ionized. This is precisely what we observe in our Fig. 4a, where the [O I] 6300 Å emission is absent in the wings but strong at the head. The [O I] emission is concentrated to the south east side of the head, roughly directed away from θ^1 Ori C. Evidences of a trapped ionization front were also obtained in the case of HH 202 (Mesa-Delgado et al. 2009a,b), located at the north west of θ^1 Ori C. In HH 202, the stronger [O I] 6300 Å emission is also located in the direction away from the Trapezium stars.

Due to the fact of having a trapped ionization front and following Mesa-Delgado et al. (2009b), we can estimate the width of the ionized slab of HH 204 and its physical separation with respect to the main ionization source, θ^1 Ori C. In our case, the ionized slab was computed from the maximum emission profiles of O^0 and He^+ with an angular distance on the plane of sky of about 2.9 ± 0.5 arcsec. Using the distance to the Orion Nebula obtained by Menten et al. (2007), $d = 414 \pm 7$ pc, and the inclination angle of HH 204 with respect to the plane of the sky calculated by O'Dell & Henney (2008a), $\Theta = 26^o$, we estimate $(6.1 \pm 1.2) \times 10^{-3}$ pc for the width of the ionized slab. To trap the ionization front the incident Lyman continuum flux must be balanced by the recombination in the ionized slab, resulting in a physical separation of $D = 0.37 \pm 0.10$ pc for the $n_e([S\ II])$ of the head (see Table 1). This result suggests that HH 204 is embedded within the body of the Orion Nebula and, therefore, discards the origin of the ionized front as result of the interaction of the gas flow with the veil, which is between 1 and 3 pc (Abel et al. 2004). If we consider the same ion (from O^0 to O^+) to compute the ionized slab $((2.9 \pm 1.2) \times 10^{-3}$ pc), the physical separation is about $D = 0.53 \pm 0.17$.

5.2   The high-temperature arc at HH 204

In the models of photoionized HH jets of Raga & Reipurth (2004), the temperature along the HH object is the typical of a gas in photoionization equilibrium —about 10^4 K— but larger at the leading working surface of the bow shock because of shock heating. This high-temperature zone is narrow and precedes the area of high-density shocked gas behind the working surface. The high-temperature arc we see in Fig. 5a may very likely correspond to that predicted structure. In fact, the arc delineates the outer edge of the bow shock and precedes the high-density compressed zone that forms the head of HH 204 as we see in Fig. 5. The upper limit for the width of the arc is $1''$, which corresponds to a linear dimension of $\sim 6 \times 10^{15}$ cm at the distance of

the Orion Nebula. The models of Masciadri & Raga (2001) —more appropriate for the Orion Nebula conditions— predict a high-temperature zone at the leading working surface with a width of the order of $\sim 4 \times 10^{15}$ cm, in a good agreement with our result.

There is a previous example of a similar structure in the literature. Based on spatially resolved echelle spectroscopy, Solf, Böhm & Raga (1988) reported a steep peak of the $T_e([C\ I])$ just at the leading edge of the bow shock of the prototypical HH 1, showing values as high as 2×10^4 K in a region about $1''$ wide. Because HH 1 belongs to the star-forming region Lynds 1641 —located at the Orion Nebula Cluster— the linear dimensions of this high-temperature zone is rather similar to that we estimate for HH 204. Solf, Böhm & Raga (1988) finds that the spatial changes of electron temperature are far much less pronounced for other ions, specially in the case of $T_e([N\ II])$, which shows hardly any variation. An important difference between HH 1 and HH 204 is that the gas excitation mechanism in both objects are completely different, pure shock excitation in the case of HH 1 and photoionization in the case of HH 204.

The high-temperature arc at the leading edge of HH 204 is a real feature and not an artifact because it can also be seen in the long-slit data of Mesa-Delgado, Esteban & García-Rojas (2008). In Figs. 7a and b we show the spatial profiles of $n_e([S\ II])$ and $T_e([N\ II])$ (Fig. 7a) and the O abundance (Fig. 7b) of a small section along the slit position 3 of Mesa-Delgado, Esteban & García-Rojas (2008) crossing the head of HH 204. That slit passes through approximately the middle of the high-temperature arc. In Fig. 7a, we can see that the $T_e([N\ II])$ peak is $2.5''$ ahead the $n_e([S\ II])$ maximum and that the $T_e([N\ II])$ peak coincides with a minimum of the total O abundance, just the effect observed in our PMAS data (see Fig. 6c). For comparison, in Figs. 7c and d we show the spatial profiles of $n_e([S\ II])$, $T_e([N\ II])$ and O abundance obtained from a pseudo-slit $-1''$ wide— obtained along the main diagonal of our PMAS maps, which is rather close to slit position 3 of Mesa-Delgado, Esteban & García-Rojas (2008). The similar behaviour of both sets of profiles is remarkable.

6   CONCLUSIONS

In this paper we analyse integral field optical spectroscopy of the area encompassing the head of the bow shock of the conspicuous Herbig-Haro object of the Orion Nebula: HH 204. We have mapped emission line fluxes and ratios, physical conditions, and ionic and total O abundances at spatial scales of $1''$.

The maps show a clear ionization stratification across the object. The presence of strong [O I] emission at the head of the bow shock and its absence at the wings indicate that those zones are optically thick and have developed a ionization front. We find evidences that HH 204 is formed within the ionized gas of the nebula and not the Veil. The head of the bow shock shows electron densities at least five times larger than the background ionized gas. We find that the density indicator based on [S II] is not providing the correct $n_e([S\ II])$ values because the nebular and auroral lines of [S II] give different ionic abundances. This is because the densities at the head are larger than the critical density. We

recompute the n_e([S II]) map solving this inconsistency and use it in the subsequent calculations.

We discover a narrow arc of high T_e([N II]) values just at the southeast edge of the head. The temperature in this zone reaches values about 1,000 K higher than in the rest of the object. This arc may correspond to structures predicted by the models of photoionized HH jets of Raga & Reipurth (2004) or Masciadri & Raga (2001), which are produced by shock heating at the leading working surface of the gas flow. The O^+ and O abundances are somewhat underestimated –between 0.1 and 0.2 dex– at this arc due to the higher temperature. We find also that the O^+ and O abundances are both about 0.1 dex larger at the northern half of the head of HH 204. Following Mesa-Delgado et al. (2011), the most likely explanation is that the appropriate density for the O^+ ion should be about 1000 cm^{-3} lower than the nominal value of n_e([S II]) assumed for those spaxels. The use of a wrong higher density produces an overestimate of the collisional de-excitation of the [O II] 3727 Å line.

The results of this paper demonstrate that the compression and heating of the gas due to high-velocity flows affect the chemical abundance determinations in H II regions. When densities reach values of the order of 10^3-10^4 cm^{-3} –as in the compressed heads of HH objects or at ionization fronts (see Mesa-Delgado et al. 2011)– the O^+ and O abundances determined from the intensity of collisional excited lines may be overestimated. Also, the presence of localized shock heating may affect the thermal balance of the gas producing artificial lower abundances. Fortunately, these disturbing effects can be analyzed in some detail in the Orion Nebula because of the higher spatial resolution attainable for this object due to its closeness, but it is difficult to explore in more distant objects and virtually impossible in extragalactic H II regions. Similar studies of larger areas of the Orion Nebula are necessary in order to: a) quantify how these localized effects can affect integrated abundance determinations when spatially resolved observations are not possible in distant objects, and b) prove whether these features could be the origin —or mimic the effects— of the so-called temperature fluctuations (Peimbert 1967). Finally, it must be remarked that abundance determinations based on recombination line ratios —which are almost independent the adopted n_e and T_e— are virtually unaffected by these disturbing effects.

REFERENCES

Abel N. P., Brogan C. L., Ferland G. J., O'Dell C. R., Shaw G., Troland T. H., 2004, ApJ, 609, 247
Bally J., Reipurth B., 2001, ApJ, 546, 299

Blagrave K. P. M., Martin P. G., Baldwin J. A., 2006, ApJ, 644, 1006
Blagrave K. P. M., Martin P. G., Rubin R. H., Dufour R. J., Baldwin J. A., Hester J. J., Walter D. K., 2007, ApJ, 655, 299
Cantó J., Goudis C., Johnson P. G., Meaburn J., 1980, A&A, 85, 128
Costero R., Peimbert M., 1970, BOTT, 5, 229
Cox D. P., Raymond J. C., 1985, ApJ, 298, 651
Cudworth K. M., Stone R. C., 1977, PASP, 89, 627
Doi T., O'Dell C. R., Hartigan P., 2004, AJ, 127, 3456
Doi T., O'Dell C. R., Hartigan P., 2002, AJ, 124, 445
Eislöffel J., Mündt R., Böhm K.-H., 1994, AJ, 108, 1042
Esteban C., Peimbert M., García-Rojas J., Ruiz M. T., Peimbert A., Rodríguez M., 2004, MNRAS, 355, 229
Esteban C., Peimbert M., Torres-Peimbert S., Escalante V., 1998, MNRAS, 295, 401
Filippenko A. V., 1982, PASP, 94, 715
García-Díaz M. T., Henney W. J., 2007, AJ, 133, 952
García-Rojas J., Peña M., Peimbert A., 2009, A&A, 496, 139
Haro G., 1952, ApJ, 115, 572
Henney W. J., 1996, RMxAA, 32, 3
Herbig G. H., Jones B. F., 1981, AJ, 86, 1232
Herbig G. H., 1951, ApJ, 113, 697
Hu X., 1996, AJ, 112, 2712
Johansson S., Zethson T., Hartman H., Ekberg J. O., Ishibashi K., Davidson K., Gull T., 2000, A&A, 361, 977
Martí J., Rodríguez L. F., Reipurth B., 1993, ApJ, 416, 208
Masciadri E., Raga A. C., 2001, A&A, 376, 1073
Menten K. M., Reid M. J., Forbrich J., Brunthaler A., 2007, A&A, 474, 515
Mesa-Delgado A., Esteban C., García-Rojas J., Luridiana V., Bautista M., Rodríguez M., López-Martín L., Peimbert M., 2009a, MNRAS, 395, 855
Mesa-Delgado A., López-Martín L., Esteban C., García-Rojas J., Luridiana V., 2009b, MNRAS, 394, 693
Mesa-Delgado A., Núñez-Díaz M., Esteban C., López-Martín L., García-Rojas J., 2011, arXiv, arXiv:1106.3602
Mesa-Delgado A., Esteban C., García-Rojas J., 2008, ApJ, 675, 389
Münch G., Wilson O. C., 1962, ZA, 56, 127
Münch G., Taylor K., 1974, ApJ, 192, L93
O'Dell C. R., 2001, ARA&A, 39, 99
O'Dell C. R., Hartigan P., Bally J., Morse J. A., 1997a, AJ, 114, 2016
O'Dell C. R., Hartigan P., Lane W. M., Wong S. K., Burton M. G., Raymond J., Axon D. J., 1997b, AJ, 114, 730
O'Dell C. R., Henney W. J., 2008a, AJ, 136, 1566
O'Dell C. R., Muench A., Smith N., Zapata L., 2008b, in Handbook of Star Forming Regions, Vol. I: The Northern Sky ASP Monograph Publications, ed. B. Reipurth, 4, 544
O'Dell C. R., Wen Z., Hu X., 1993, ApJ, 410, 696
O'Dell C. R., Wong K., 1996, AJ, 111, 846
O'Dell C. R., Yusef-Zadeh F., 2000, AJ, 120, 382
Oke J. B., 1990, AJ, 99, 1621
Peimbert M., 1967, ApJ, 150, 825
Pogge R. W., Owen J. M., Atwood B., 1992, ApJ, 399, 147
Quinet P., 1996, A&AS, 116, 573
Raga A., López-Martín L., Binette L., et al., 2000, MNRAS, 314, 681

Raga A. C., Reipurth B., 2004, RMxAA, 40, 15

Raga A. C., Riera A., González-Gómez D. I., 2010, A&A, 517, A20

Reipurth B., Bally J., Fesen R. A., Devine D., 1998, Natur, 396, 343

Reipurth B., Raga A. C., Heathcote S., 1992, ApJ, 392, 145

Riera A., Phillips J. P., Mampaso A., 1990, Ap&SS, 171, 231

Rosado M., de La Fuente E., Arias L., Le Coarer E., 2002, RMxAC, 13, 90

Rosado M., de la Fuente E., Arias L., Raga A., Le Coarer E., 2001, AJ, 122, 1928

Roth M. M., Kelz A., Fechner T., et al., 2005, PASP, 117, 620

Schwartz R. D., Dopita M. A., 1980, ApJ, 236, 543

Simón-Díaz S., Herrero A., Esteban C., Najarro F., 2006, A&A, 448, 351

Simón-Díaz S., Stasińska G., 2011, A&A, 526, A48

Solf J., Böhm K. H., Raga A., 1988, ApJ, 334, 229

Storey P. J., Hummer D. G., 1995, MNRAS, 272, 41

Taylor K., Munch G., 1978, A&A, 70, 359

Walsh J. R., 1982, MNRAS, 201, 561

Zhang H., 1996, A&AS, 119, 523